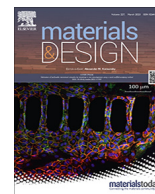




Contents lists available at ScienceDirect

Materials & Design

journal homepage: www.elsevier.com/locate/matdes



Investigation of the structure and ionic conductivity of a Li_3InCl_6 modified by dry room annealing for solid-state Li-ion battery applications

Palanivel Molaiyan^{a,*,1}, Sarah E. Mailhiot^{b,1}, Kevin Voges^{c,d,1}, Anu M. Kantola^b, Tao Hu^a, Peter Michalowski^{c,d}, Arno Kwade^{c,d}, Ville-Veikko Telkki^b, Ulla Lassi^{a,*}

^a Research Unit of Sustainable Chemistry, University of Oulu, 90570 Oulu, Finland

^b NMR Research Unit, University of Oulu, 90570 Oulu, Finland

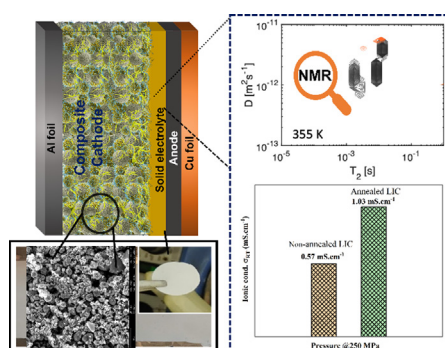
^c Institute for Particle Technology, Technische Universität Braunschweig, Volkmaroder Str, 5, 38104 Braunschweig, Germany

^d Battery LabFactory Braunschweig (BLB), Technische Universität Braunschweig, Langer Kamp, 19, 38106 Braunschweig, Germany

HIGHLIGHTS

- Simple approach for dry room annealing synthesis of Li_3InCl_6 .
- Dry room annealed monoclinic Li_3InCl_6 has an ionic conductivity of $\sim 1 \text{ mS cm}^{-1}$.
- NMR studies revealed the effect of impurities on Li^+ diffusion.
- Processing challenges of Li_3InCl_6 HSE as catholyte in solid state batteries are addressed.

GRAPHICAL ABSTRACT



ARTICLE INFO

Article history:

Received 14 October 2022

Revised 30 January 2023

Accepted 1 February 2023

Available online 6 February 2023

Keywords:

Halide solid electrolyte

Li diffusion

Ionic conductivity

Processing challenges

Solid-state batteries

ABSTRACT

Progress in new sustainable technologies depends on the development of battery materials, specifically on safer, low-cost, and higher energy density batteries. One new type of materials are the halide solid electrolytes (HSEs), which have been shown to exhibit high ionic conductivity, deformability, and oxidative stability. Here, the synthesis of Li_3InCl_6 (LIC) HSEs by ball-milling followed by dry room annealing is investigated. Crystal structure, particle size, and ionic conductivity are analyzed using a combination of X-ray diffraction, transmission electron microscopy, and electrochemical impedance spectroscopy. Dry room annealing increases the presence of impurities in the sample but also increases the Li^+ ionic conductivity up to 1.03 mS cm^{-1} . Additional pulsed-field gradient and relaxation time NMR measurements were performed to understand the lithium diffusion in the LIC samples. Two-dimensional diffusion – T_2 relaxation correlation and T_2 relaxation exchange measurements showed that there are multiple unique Li atomic motion sites, which are correlated to different rates of diffusive, micrometer-scale motion. This work outlines a simple solid-state synthesis approach and a novel strategy for designing advanced materials, understanding the ionic conduction, as well as the challenges in scalable wet processing of halide-based cathode sheets for solid-state battery applications.

© 2023 The Authors. Published by Elsevier Ltd. This is an open access article under the CC BY license (<http://creativecommons.org/licenses/by/4.0/>).

* Corresponding authors. Address: Faculty of Technology, Research Unit of Sustainable Chemistry, University of Oulu, Pentti Kaiteran katu 1, 90570 Oulu, Finland.

E-mail addresses: palanivipphys87@gmail.com (P. Molaiyan), ulla.lassi@oulu.fi (U. Lassi).

¹ These authors have the same contribution to this paper.

1. Introduction

Combusting fossil fuels for transportation significantly contributes to global CO₂ emissions. Therefore, there is a need for transition from traditional automobiles to electric vehicles with high energy-density batteries [1]. Developing these sustainable technologies require batteries that last longer, charge faster, and are safer and more sustainable [2,3]. Lithium-ion batteries (LIBs) are currently the best-performing technology for energy storage. Nonetheless, they suffer from safety issues due to increasingly sensitive materials and flammable liquid electrolytes. One approach to overcome these safety concerns is switching from liquid- to solid electrolytes (SEs) [4]. Solid-state batteries (SSBs) utilize SEs instead of traditional liquid organic electrolytes and therefore offer potential advantages in safety and costs, as well as in thermal and electrochemical stability [5,6]. Furthermore, SEs offer high ionic conductivity, high energy density, longer lifespan, and excellent reliability [7,8]. Several types of SEs such as oxide-based Li_{3x}-La_{2/3-x}TiO₃ and Li₇La₃Zr₂O₁₂, sulfide-based Li₂S-P₂S₅ and Li₁₀GeP₂-S₁₂ (LGPS), halide-based Li₃MCl₆ (M = In, Y, Er), hydride-based Li₂B₁₂H₁₂, polymers (Polyethylene oxide, PVDF-HFP), and thin-film (LiPON) SEs have been considered as promising candidates for next-generation SSBs [3,7,9,10]. Notably, several sulfide SEs such as LGPS have been reported to deliver ultrahigh ionic conductivity (over 10 mS cm⁻¹) at room temperature (RT). This is comparable with current liquid electrolytes used in LIBs [11]. Kanno et al. showed that Li_{9.54}Si_{1.74}P_{1.44}S_{11.7}Cl_{0.3} has the highest ionic conductivity (25 mS cm⁻¹) reported for LGPS-type materials [12]. However, sulfide SEs face challenges in processability and material handling due to the toxicity of H₂S gas formation. On the other hand, oxide and polymer SEs have lower ionic conductivities and need more investigation to improve their performance. The main challenges in SSB research are the design of high-performance SEs as well as the development of scalable production and facile processing methods to transfer the technology into the market [13].

Halide solid electrolytes (HSEs) have gained attention recently due to their simple synthesis, relatively high ionic conductivity, and good processability. Halide-based SEs were recently found to exhibit desirable sulfide, polymer, and oxide systems characteristics, including deformability and oxidative stability. The general formula of HSEs is Li₃MX₆ (M = Y, In, Er, Sc, etc.), and the crystal structure depends on the doping of different metals with halogen compounds (X = F, Cl, Br, I) [14,15]. Examples include monoclinic Li₃InCl₆ (ionic conductivity ~2 mS cm⁻¹ at RT) [16,17], orthorhombic Li_{3-x}M_{1-x}Zr_xCl₆ (M = Y, Er, ~1.4 mS cm⁻¹) [14,18], spinel Li₂-Sc_{2/3}Cl₄ (1.5 mS cm⁻¹) [19], monoclinic Li_xScCl_{3+x} (3 mS cm⁻¹) [20], and trigonal Fe³⁺-substituted Li₂ZrCl₆ (1 mS cm⁻¹) [21]. Two different HSEs were also reported, Li₃InCl₆ (LIC) [22] and Li₃YCl₆ (LYC) [23], which have monoclinic (C2/m) and trigonal (P3m1) structures, respectively. These HSEs show relatively high ionic conductivities, 0.71 and 0.65 mS cm⁻¹ for ball milled powders of LIC and LYC, respectively. Two different HSEs, Li₃YCl₆ and Li₃YBr₆, were synthesized via ball-milling followed by annealing and offered high ionic conductivity, electrochemical and chemical stability, and deformability [14]. Nazar's group has observed a metastable trigonal phase of Li₃YbCl₆ with an ionic conductivity of 0.1 mS cm⁻¹ and mixed-metal HSEs, Li_{3-x}Yb_{1-x}Zr_xCl₆, with conductivities up to 1.1 mS cm⁻¹ at RT, which is higher than for LYC [24]. Interestingly, the ionic conductivity of a Li₂ZrCl₆ (LZC) was reported to be 0.81 mS cm⁻¹ at RT and its compatibility with high voltage cathodes was demonstrated. Additionally, LZC is also a promising cost-effective material compared to In and Y, with a humidity tolerance (relative humidity RH = 5 %) and low conductivity degradation after exposure to atmosphere [25].

Li et al. [26] reported that the water-mediated synthesis of LIC partially forms Li₃InCl₆·2H₂O, and the ionic conductivity of the LIC is 2 mS cm⁻¹. However, after the sample was exposed to low relative humidity (5 %) with different time durations, the ionic conductivity decreased by several orders of magnitude. Recently, Wang et al. [27] studied the impact of varying air exposure times on the degradation mechanisms of LIC and LYC (RH of 30–70 %). They reported that both HSEs quickly absorb water and form a crystalline hydrate, which is then partially decomposed to InCl₃ and LiCl. Later, InCl₃ further hydrolyzes, producing acid, and creating In₂O₃ impurities [27]. To improve the air stability of the HSEs, they coated the surface with Al₂O₃ by atomic layer deposition.

The high sensitivity of HSEs to moisture requires strict humidity control in synthesis, storage, and transportation, which increases the application costs. Therefore, the stability of HSEs in air is a crucial concern. So far, most studies have focused on improving the ionic conductivity of HSEs, but less attention has been paid to air stability. In this work, the structure and properties of a ball milled (hereafter referred as *non-annealed*), and the dry room annealed LIC HSEs (hereafter referred to as *annealed*) is studied by various advanced characterization techniques. A combination of X-ray diffraction (XRD), electrochemical impedance spectroscopy (EIS), and pulsed-field gradient nuclear magnetic resonance (PFG NMR) spectroscopy provides a multiscale understanding of ion diffusion processes, ionic conductivity, and crystallinity of the LIC. To improve resolution and understanding of diffusive behavior over a wider range of time scales, PFG NMR measurements are paired with T₂, D-T₂ correlations, and T₂-T₂ exchange measurements. This work also provides an insight into challenges regarding a scalable wet processing of the material as catholyte for SSB cathodes and guides the future design for the development of new HSEs.

2. Material and methods

2.1. Preparation of Li₃InCl₆

The Li₃InCl₆ (LIC) solid electrolyte materials were synthesized by the high-energy ball milling method (Emax, RETSCH GmbH, Germany). The starting materials lithium chloride (LiCl, Alfa Aesar, 99.9 %) and indium chloride (InCl₃, Alfa Aesar, 99.99 %) were mixed with a stoichiometric molar ratio of 3:1. The materials were placed into Zirconia vials (internal volume of 125 mL) locked in vacuum-sealed containers together with zirconia balls with a ball-to-powder (mass) ratio of 17:1. The synthesis of Li₃InCl₆ materials worked with a milling speed of 500 rpm, media size of 5 mm, milling time of 24 h, material weight of 8 g, milling media weight of 135 g and an internal water-cooling circuit (10 °C) during the milling process. The as-milled powders were collected and pelletized inside the Argon glove box (Ar). 600–800 mg powders were pressed into compacted pellets using a hot press to form a pellet inside the Ar glove box with a force of 200 MPa for 60 s in a 16 mm stainless steel mould. The pellets were annealed at 260 °C, with a heating rate of 5 °C min⁻¹ for 5 h in a dry room atmosphere. The dry room had a relative humidity of 0.5 % and a dew point -45 °C. The colourless pellets were ground by mortar and pestle into powders that were used for subsequent characterization.

2.2. Structural and morphology characterization

The non-annealed and annealed LIC materials were characterized by X-ray diffraction (XRD) using a PANalytical X'Pert Pro X-ray diffraction with CuKα (λ₁ = 1.5406 Å) with the variable slit. The XRD data were collected from 10 to 90° (2θ) and scanned 90 s per step with one step of 0.017°. The samples were placed

in airtight XRD holders covered in Kapton foil to prevent moisture from the air affecting the sample. The structural parameters and phases of the LIC were determined by the Rietveld refinement (WPPF method) using PDXL2 software and International Centre for Diffraction Data (ICDD, PDF-4+ 2022 RDB) database. The morphologies of non-annealed LIC HSEs powders were characterized by a Hitachi S-4800 field emission scanning electron microscopy (FESEM) equipped with energy dispersive spectroscopy (EDS). The morphology and microstructure of the LIC particles were also studied using an energy filtered transmission electron microscope (EFTEM) with scanning transmission electron microscopy (STEM), JEOL JEM-2200FS EFTEM/STEM (JEOL Ltd. 3-1-2 Musashino, Akishima, Tokyo 196-8558, Japan). The sample powders were placed on a 200-mesh copper grid pre-coated with carbon (Lacey C, TED PELLA, INC.). The accelerating voltage and emission current in the measurements were 120 kV and 8–15 μ A. The SAED diffraction pattern generated by TEM was analyzed by CrysTBox program. The particle size of the samples was measured from TEM image using Fiji program and gave a reasonable particle size distribution.

2.3. X-ray photoelectron spectroscopy (XPS)

XPS analysis was performed using a Thermo Fisher Scientific ESCALAB 250Xi XPS System (Thermo Fisher Scientific, 168 Third Avenue, Waltham, MA USA 02451) at the Centre for Material Analysis, University of Oulu, Finland. The powder samples were placed on a gold sample holder. The high-resolution scan used pass energy of 20 eV while the survey scan used pass energy of 150 eV. The monochromatic AlK α radiation (1486.7 eV) operated at 20 mA and 15 kV with X-ray spot size of 900 μ m. The Li, In, O, Cl and C were measured for all samples and the measurement data were analyzed by Advantage V5 program. The charge compensation was carried out by applying the C1s at 284.8 eV as a reference to determine the presented spectra and calibrate the binding energies.

2.4. Electrochemical impedance spectroscopy (EIS)

The ionic conductivities of the LIC materials were measured using electrochemical impedance spectroscopy (EIS) from ZENNIUM, Zahner, Germany. Impedance measurements were performed on non-annealed and annealed of LIC (250–300 mg) powders filled into custom-designed (\varnothing = 16 mm) Teflon holders. The blocking electrodes were prepared by stainless steel cylinders in a stainless steel /LIC/ stainless steel configuration and applied at different pressures to obtain ionic conductivity at room temperature. The thickness was about 1 mm, and the diameter of the pellets was 16 mm. The ionic resistance data was collected from 10 Hz to 4 MHz frequency range and an applied amplitude of 10 mV.

2.5. NMR measurements

NMR measurements were performed using a 14.1 T Bruker AVANCE III spectrometer equipped with a 5 mm BBO Diff probe with a maximum gradient strength of 17.4 Tm $^{-1}$ (Bruker, Billerica, MA, USA). Diffusion measurements were performed using a pulsed gradient stimulated echo (PGStE) pulse program [28] with 3 ms gradient duration δ , smooth square gradient shape, 4.3 ms echo time, and 16 gradient amplitudes from 0.85 to 17.07 Tm $^{-1}$. The diffusion time Δ was varied from 10 to 150 ms at 355 K. Temperature-dependent D (Δ = 10 ms) data were taken from 295 to 355 K with 10 K increments. A temperature stabilization delay of 60 min was used between scans. Data was taken using 16 scans with a scan delay of 10 s. The experiment time for a single Δ was 43 min. Data was fit with a single exponential fit in Matlab (Mathworks, Natwick, MA, USA, R2021a).

T_2 measurements were carried out using a Carr-Purcell-Meiboom-Gill (CPMG) pulse sequence [29] with an echo time of 200 μ s and 150 echoes. Echo data were collected in the center of each echo. Data were taken using 8 scans with a scan delay of 100 s. The experiment time was 45 min. Data were taken from 245 to 355 K with 10 K increments. A heating delay of 60 min was used between scans. Data was fit with a biexponential fit in Matlab. D - T_2 measurements were made using a 2D pulse program consisting of a PGStE block with variable gradient strength, followed by a CPMG sequence [30]. An echo time of 200 μ s and 300 echoes were used in the CPMG sequence. PFG encoding was performed with 3 ms gradient duration δ , smooth square gradient shape, 4.3 ms echo time, and 64 gradient amplitudes from 0.53 to 17.07 Tm $^{-1}$. Data were taken using 64 scans with a scan delay of 10 s. The experiment time was 12 h. Data were taken at 355 K. Data were analyzed with the 2D Inverse Laplace transformation [31]. T_2 - T_2 measurements were performed using a 2D pulse program consisting of a CPMG block with variable number of echoes, a mixing time, and a CPMG sequence [32]. An echo time of 200 μ s was used. In the indirect dimension, the number of echoes were varied from 2 to 150 echoes with 64 steps. The direct dimension recorded data from 300 echoes. The mixing time was set to 1, 10, 100, and 250 ms. Data were taken using 4 scans with a scan delay of 20 s. The experiment time was 90 min and the measurement temperature 355 K. The data were analyzed with the 2D Inverse Laplace transformation.

2.6. Catholyte process

For the commercialization of this technology, a scalable processing route is a prerequisite for potential industrialization of halide SSB production. Therefore, we conducted simple but scalable slurry-based coating experiments to produce sheet-type composite cathodes by methods that are close to the production of conventional LIBs. The synthesized Li₃InCl₆ powders (27 wt%) together with 67 wt% NCM622, 3 wt% conductive additive (Super C65), and 3 wt% of the polymeric binder were dispersed in a solvent by ball-milling (400 rpm for 30 min). Two different binder-solvent combinations were tested – hydrogenated nitrile butadiene rubber (HNBR) in p-xylene as well as polyisobutylene (PIB) in toluene – that were already successfully used for sulfide-based SSB production [33]. The as-prepared cathode slurries were then coated on aluminium substrate (Al foil) by doctor blading (300 μ m) on a film applicator and subsequently dried at 70 °C on the heating plate of the film applicator for 30 min. On top of the dried cathode sheets, the second coating of pure SE and 5 wt% of binder was applied as a separator layer (500 μ m) and dried at room temperature. These bilayer sheets were then cut to shape for further analysis.

3. Results and discussion

3.1. Materials synthesis

LIC samples were synthesized by mechanochemical milling of stoichiometric amounts (3:1) of LiCl and InCl₃ precursors, followed by high-temperature heat treatment at 260 °C for 5 h at dry room conditions. This work introduces the dry room annealing process for the first time to LIC materials as illustrated in Fig. 1a. The dry room has a relative humidity (RH) of below 1 % and a dew point of around –45 °C (\sim 0.5 % H₂O). It has been favourable for processing and handling halide-based materials for low humidity tolerance [22,27].

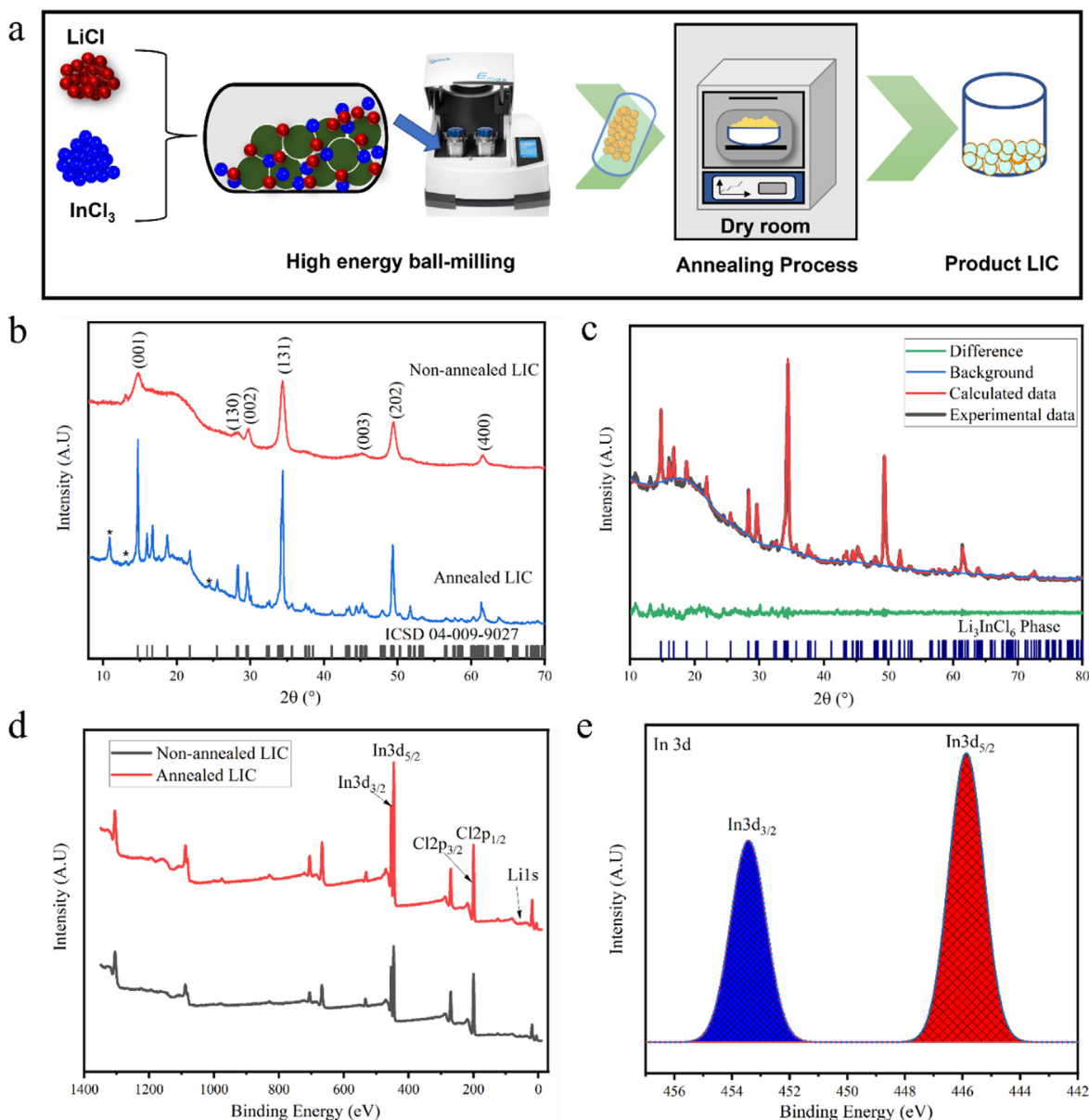


Fig. 1. (a) Schematics of the synthesis of the LIC solid electrolytes, including ball-milling followed by an annealing step. The annealing process is carried out under dry room conditions. (b) XRD patterns of the non-annealed (ball-milled) and annealed LIC samples. InOCl impurities appearing during heating under dry room conditions are indicated by asterisks. (c) Rietveld refinement of the annealed LIC. (d) The XPS survey of non-annealed (ball-milled) and annealed LICs and (e) In 3d peaks of the non-annealed LIC.

3.2. X-ray diffraction (XRD)

The XRD results show that in both non-annealed and annealed samples, major diffraction peaks of LIC are indexed to the monoclinic structure (ICDD:04-009-9027) (Fig. 1b). The annealed sample has the majority of the pure phases of monoclinic structure comparable to the previously reported literature [16]. The impurity peaks of InOCl (ICDD: 040126277, space group of pmmn) are formed during the annealing process due to the humidity, as seen from XRD. The Rietveld refinement results (Fig. 1c) show that the annealed LIC consists of a monoclinic structure (ICSD:04-009-9027) with a space group of $\text{C}2/m$ and the expanded of 6.414 Å (a), 11.084 Å (b), and 6.390 Å (c) (Table S1). The ball-milled sample has the lattice parameters of 6.12 Å (a), 11.20 Å (b), and 6.04 Å (c).

Notably, the Li^+ ionic conductivity in halide superionic conductors is more pronounced for the monoclinic structure (higher ionic conductivity) to form than the orthorhombic structure (low ionic

conductivity) [16,17]. XPS measurements were carried out to determine the surface chemical compositions of the non-annealed and the annealed LIC samples. According to the broad survey curves of LIC (Fig. 1d), peaks corresponding to Cl 2p, In 3d, and Li 1s can be observed (Table S2). In $3d_{5/2}$ and In $3d_{3/2}$ peaks are located at 446.2 eV and 453.8 eV, respectively (Fig. 1e), which correspond to the In^{3+} bonding state of LIC that has been previously observed [17]. Also, Cl 2p spectra of pure LIC shown in Fig. S1 only indicate a pair of peaks of Cl $2p_{3/2}$ and Cl $2p_{1/2}$ at 199.6 eV and 201.2 eV, respectively, that are associated with In-Cl bonds in LIC.

3.3. Pulsed field gradient NMR (PFG NMR)

To understand Li-ion diffusion, the LIC samples were studied by PFG NMR. In SEs, the ion conduction pathways are composed of tortuous, nano-scale Li^+ channels through which Li^+ diffuses. PFG NMR is a non-invasive, multi-scale method for quantifying the

apparent self-diffusion coefficient D , and in SEs ^7Li D studies can be used to understand ion conduction mechanisms [34]. Another measure for how Li moves across the structure is temperature-dependent D at the shortest diffusion time ($\Delta = 10$ ms). At all temperatures, Li diffuses more quickly in the annealed LIC than in the non-annealed LIC (Fig. 2c), and the diffusion activation energy is smaller in the annealed LIC ($E_a = 1.3 \pm 0.1$ kJ mol $^{-1}$) than in the non-annealed LIC ($E_a = 1.7 \pm 0.1$ kJ mol $^{-1}$). Since Li-ion transport is facilitated by impurities [37], which were observed in XRD data (Fig. 1b), it can be concluded that micrometer Li ion transport is more efficient in the annealed sample due to the increase in impurities.

In SEs, ^7Li NMR T_1 and T_2 relaxation times have been shown to relate to atomic-scale Li motion [38,39,40,41]. T_2 relaxation times reflect the local physical and chemical environments such that a shorter T_2 represents a reduced hopping rate of Li between atomic sites in a crystal lattices and defects, i.e., reduced mobility of Li. Both the non-annealed and annealed LIC samples have two T_2 relaxation components, one with T_2 below 1 ms (Fig. 3a) and the other with T_2 ranging from 1 to 10 ms (Fig. 3b). The values agree with reported range of T_2 times (0.1–4 ms) of other SEs [36,42]. We interpret that the two components arise from Li ions in two different chemical environments. In principle, it is also possible that the two different T_2 times originate from sample regions with different magnetic field homogeneities, however, this is unlikely as the samples are homogenous powders and the magnetic field was shimmed such that the linewidths were relatively narrow (3 and 6 kHz at 300 K for non-annealed and annealed LICs, respectively). In the non-annealed sample, both T_2 times increase with temperature, resembling typical Arrhenius-type behavior. However, T_2 times of the annealed samples behaves differently, showing a maximum at around 270 K and indicating different atomic level mobility and surrounding for Li. The low temperature T_2 values are attributed to the strength of interaction between Li and its environment [35], and the higher T_2 values indicate weaker interactions in the annealed sample.

To improve resolution and increase information content of relaxation and diffusion experiments, 2D NMR methods can be used such as D - T_2 correlations [43]. ^7Li D - T_2 correlates micrometer scale Li motion with atomic scale interactions between Li and its environment. In both non-annealed and annealed LIC samples, D - T_2 probability distributions show two D components associated with the two T_2 components (Fig. 3c). These D components were not separated in 1D measurements, however, both fall within the width of the 1D D probability distribution. Additionally, the signal intensities of the 2D D - T_2 measurements correspond to the independently measured T_2 probability distribution signal intensities. Therefore, it can be concluded that there are two rates of Li D within both LIC samples correlated with different chemical environments.

A second 2D NMR method, ^7Li T_2 relaxation exchange spectroscopy (REXSY) [32], provides additional insights on the micro-scale motion of Li ions. In the REXSY experiment, T_2 is measured before and after a mixing time τ_m . In this experiment, the Li displacement z scales with the mixing time such that $\langle z^2 \rangle = 2D\tau_m$. In the 2D T_2 - T_2 probability distributions, the signal intensity of the off-diagonal peaks represents the number of spins that moved between two chemical environments characterized by the T_2 values of the two dimensions. Both samples show exchange between the two T_2 sites of around 1 and 10 ms at the longest mixing time of 100 ms (Fig. 4). Furthermore, the non-annealed sample shows an indication of exchange with a third site characterized by a very short T_2 value (about 0.2 ms), potentially corresponding to highly immobile Li atoms. However, this site is not probed very reliably in the experiments as the T_2 of the site is equal to or shorter than

the CPMG echo time. These two 2D NMR methods together indicate that diffusive, micrometer motion is occurring such that Li is moving between different chemical environments, such as grain boundaries, impurities, Schottky defects, and Frenkel defects [38] and that this motion is affected by annealing and the introduction of impurities.

3.4. Morphology and ionic conductivity studies

The scanning electron microscopy (SEM) image of the non-annealed LIC sample (Fig. 5a) shows features in the 2–5 μm range and finger-type morphology. The EDS mapping shows homogenous elemental distributions of In (20 %) and Cl (80 %), suggesting that the uniform LIC is formed (Fig. S2). To understand more about LIC morphology, transmission electron microscopy (TEM) was used. Fig. 5b–c indicates that the orientation of crystal is 1.98 Å (3,1,0), 1.82 Å (2,0,2) and 1.58 Å (4,0,–82) and layered structure seen in Fig. S3. The mean particle size calculated from the TEM images are 12 (Fig. 5d) and 30 nm (Fig. S3) for the non-annealed and annealed LIC, respectively.

Ionic conductivities of the non-annealed and annealed LIC samples were characterized using pressure-dependent EIS. The Nyquist plots of the non-annealed LIC sample with different pressures applied from 150 to 275 MPa at RT are shown in Fig. 5e. The resistance of the non-annealed LIC at RT vary between 100 Ω (150 MPa) and 85 Ω (275 MPa) (Fig. 5f), resulting in corresponding conductivities of 0.485 and 0.55 mS/cm, respectively. The grains have less contact at the lower pressures, resulting in lower conductivity, while higher pressure improves ionic conductivity. Dry room annealing improves the ionic conductivity (Fig. 5f) by a factor of 2. Compared with different synthesis methods (Table S3) [17,26], our approach based on the dry room annealed reaches comparable ionic conductivity of 1.03 mS cm $^{-1}$ at RT (Fig. S4) and is a promising and scalable method for future applications.

3.5. Processing challenges

In terms of cell component manufacturing (composite cathodes and SE separators), the processability of LIC is similar to thiophosphate SEs. LIC has a comparatively low Young's modulus of 38 GPa [33] (similar to that of thiophosphates [44]) and it deforms plastically even at RT above a certain pressure. This allows for close particle–particle contacts of the cathode active material (CAM) and the SEs by simple pressing (e.g. [5]), which is necessary to reach a suitable performance [45]. On the laboratory scale, this is usually done by uniaxial pressing of a mixed powder bed. But these pressed pelletized cells are not scalable to an industrially relevant scale where roll-to-roll coating processes are commonly used for high-throughput production of sheet-type battery electrodes. Therefore, a similar approach was tested for LIC where all cathode components (CAM, LIC, carbon additive, and polymeric binder) were dispersed in a solvent by low-energy ball-milling and then coated on Al substrate foil via doctor blading on a film applicator. It can be seen in Fig. 6a, that p-xylene which is suitable for sulfide SEs [33] is not an appropriate solvent for LIC due to fast segregation (no stable suspension). Toluene was used in the literature [46] and was therefore utilized here as a proof-of-concept. The resulting cathode suspension was stable enough to be coated on the Al substrate (Fig. 6b). The resulting composite cathode sheets were stable enough to be handled and cut into shape. SEM images of these sheets (Fig. 6c) show a homogeneous distribution of CAM and LIC reflecting successful mixing and dispersing step. The second coating of pure LIC SE suspension (LIC and polymeric binder in toluene) on top of the cathode as separator layer was unsuccessful because the sheets teared and curled up while drying (Fig. 6d) which made

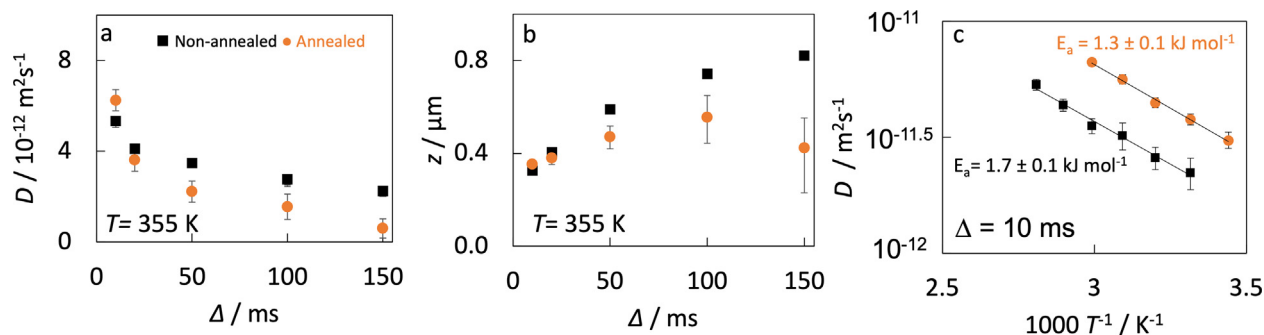


Fig. 2. (a) Diffusion coefficient of lithium ions in the LIC samples as a function of diffusion time Δ measured by ^7Li PFG NMR at 355 K and (b) the corresponding root-mean-square-displacements of the ions. (c) Diffusion coefficients as a function of temperature using a constant diffusion time of $\Delta = 10 \text{ ms}$. Data of the non-annealed and annealed LIC samples are shown by black and orange, respectively. Solid lines in (c) represent Arrhenius fits. (For interpretation of the references to colour in this figure legend, the reader is referred to the web version of this article.)

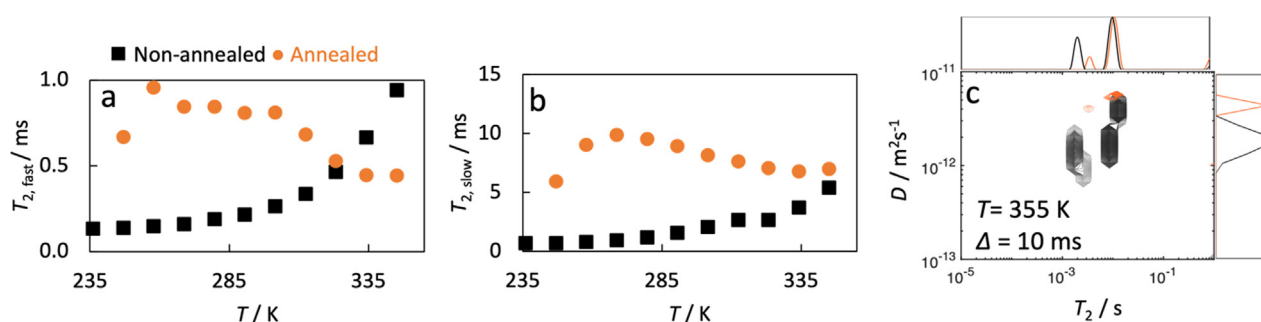


Fig. 3. ^7Li T_2 relaxation times of the (a) faster and (b) slower decaying components as a function of temperature. The values were obtained from two-component exponential fits with the experimental CPMG data. (c) 2D D - T_2 correlation probability distribution observed at 355 K along with the corresponding measured 1D D and T_2 probability distributions. Data is shown for the non-annealed (black) and annealed (orange) LICs. (For interpretation of the references to colour in this figure legend, the reader is referred to the web version of this article.)

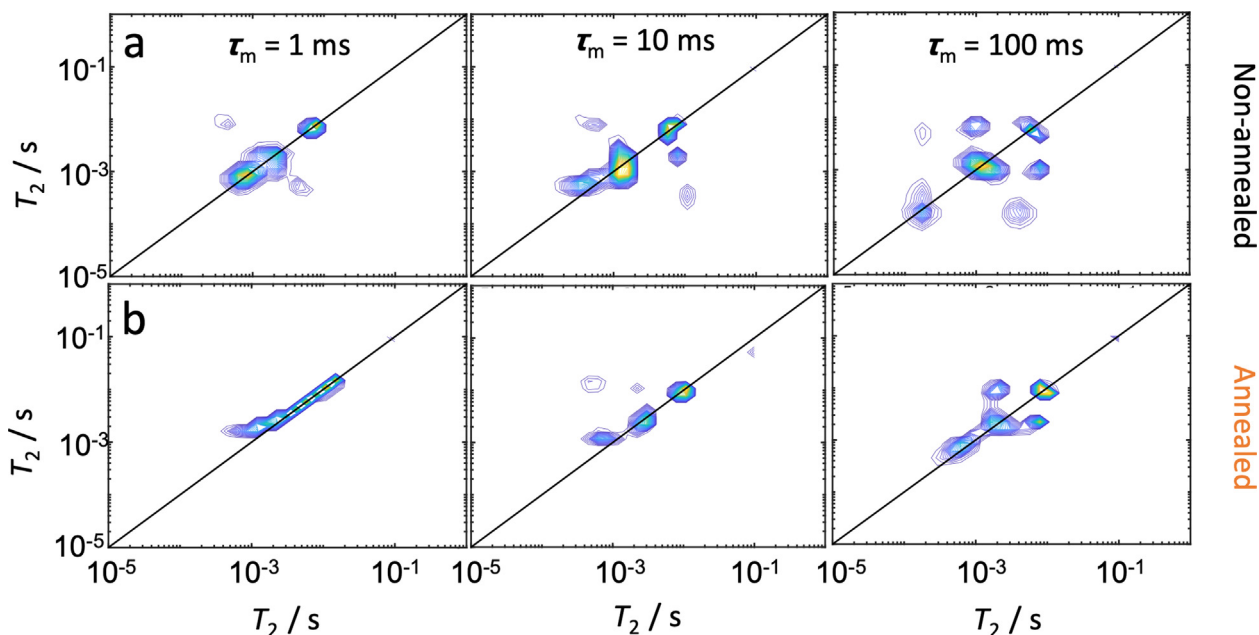


Fig. 4. 2D T_2 relaxation exchange spectroscopy probability distributions with mixing times of 1, 10, and 100 ms for the (a) non-annealed and (b) annealed LICs measured at 355 K.

it necessary to apply a Li_3PS_4 separator coating instead as a proof-of-concept. The as-prepared bilayer coatings (cathode and SE separator on Al foil) could be punched into round samples without cracking or spalling (Fig. 6e). Hence, a slurry-based production of

sheet-type LIC composite cathodes is in principle possible. Still, optimization is needed to identify the most suitable composition (e.g. LIC/CAM ratio, binder amount etc.) and process parameters (e.g. mixing intensity, coating speed etc. [13]).

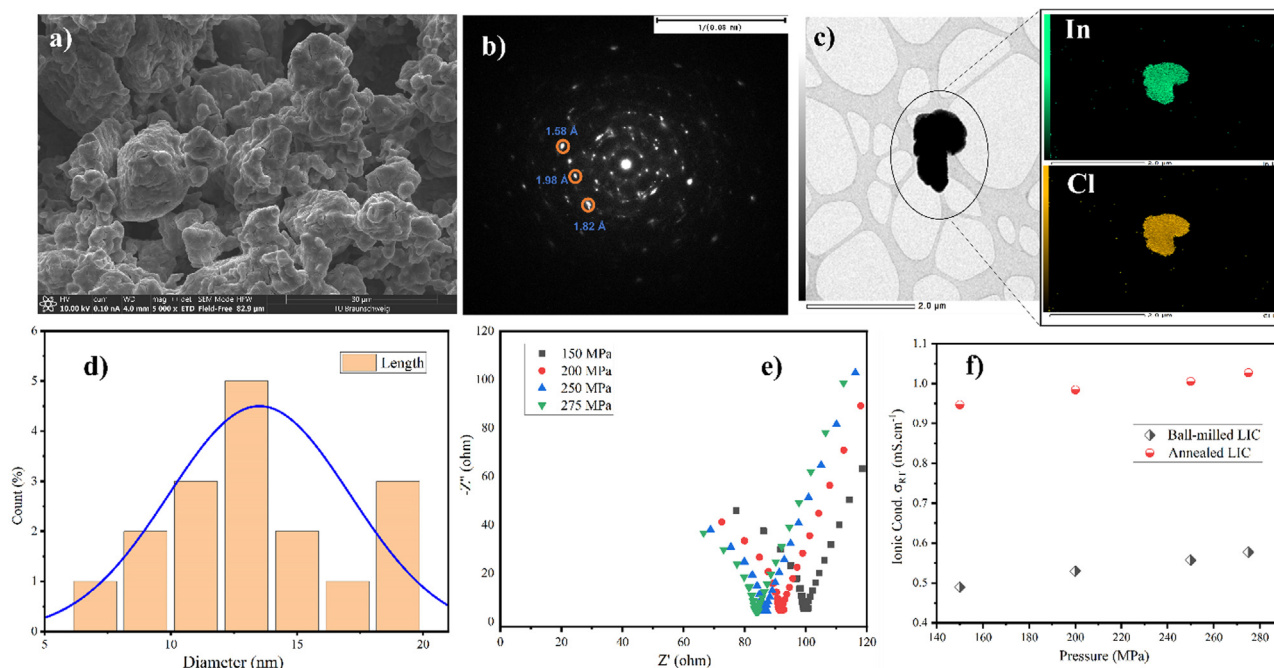


Fig. 5. (a) SEM image of the non-annealed LIC. (b) SAED pattern and (c) EDS mapping of a TEM image of the non-annealed LIC. (d) The particle size distribution of the non-annealed LIC. (e) Nyquist plots of the non-annealed LIC samples with different pressures at room temperature. (f) The ionic conductivity of the non-annealed and annealed LIC sample was applied with a pressure range of 150, 200, 250, and 275 MPa measured at room temperature.

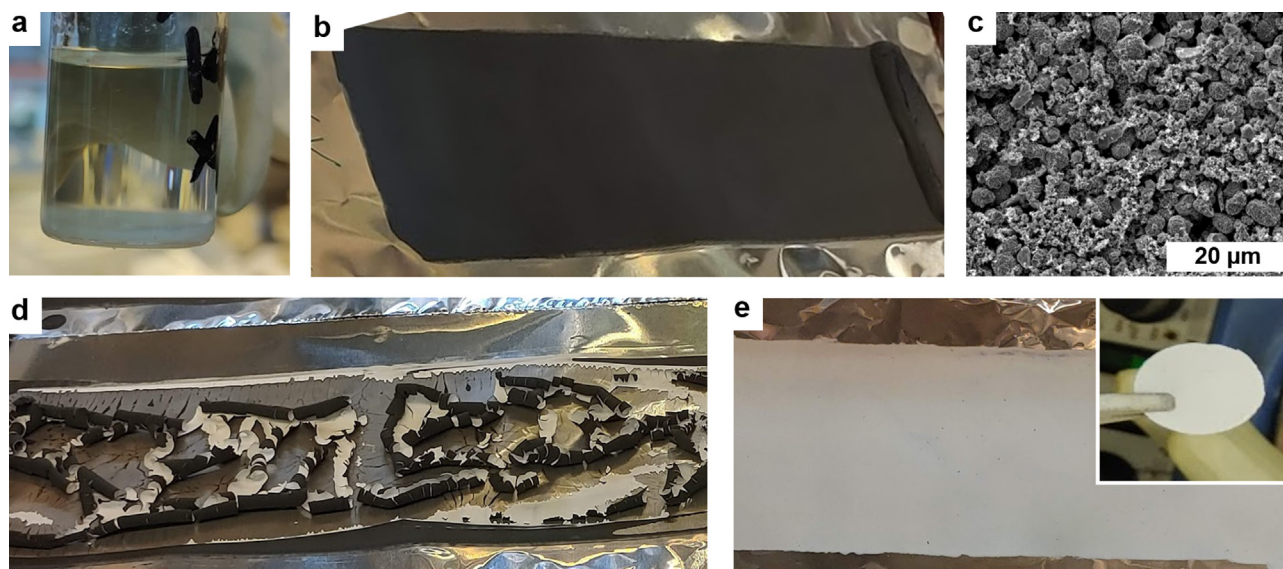


Fig. 6. (a) Segregation of LIC in p-xylene. (b) Composite cathode sheets were produced via doctor blading (67 wt% NCM622, 27 wt% LIC, 3 wt% Super C65, and 3 wt% PIB binder). (c) SEM image of composite cathode coating. (d) LIC separator coating (95 wt% LIC and 5 wt% PIB binder) on top of the as-prepared cathode revealed cracks and disintegration of the sheets. (e) Li₃PS₄ separator coating (95 wt% Li₃PS₄ (LPS) and 5 wt% HNBR binder) on top of the as-prepared cathode revealed dense and crack-free bilayer sheets that could be punched without cracking/spalling.

Another possible production route of composite cathode sheets is the infiltration of conventionally produced LIB cathodes with a SE solution, as has been already successfully shown for thiophosphate SSB cathodes [46]. Regarding sustainability and cost-effectiveness, the development of a solvent-free coating process should be considered in future investigations. Another critical point in the processing of larger halide SSB cells is the densification at elevated pressures, either by uniaxial pressing or calendaring.

Like the thiophosphate SE, the LIC containing sheets experience embrittlement above a certain pressure which makes the coatings quite stiff, and bending is almost impossible without cracking of the thin and fragile densified sheets. This is not only problematic in a roll-to-roll process where the material is rolled on coils but also for cutting the material because it may spall on the rims due to brittle failure. Therefore, the sheets would have to be cut to size before densification when they are still flexible. An elegant method

to overcome this obstacle has been shown by Zhao et al. [46], and they used glass fiber films dipped into LIC precursor solution, resulting in flexible LIC separator sheets.

4. Conclusions

In summary, this work investigates the synthesis of Li_3InCl_6 HSEs through ball-milling followed by annealing in dry room atmosphere. We analyse the crystal structure, particle size, and ionic conductivity using a combination of X-ray diffraction, electron microscopy, and electrochemical impedance spectroscopy (EIS). Additional 1D and 2D pulsed-field gradient and NMR relaxation time measurements were used to understand the lithium diffusion mechanisms of non-annealed and annealed samples. Time-dependent diffusion measurements show short-range motion within the grains in both samples and indicate that grain size is reduced after annealing. In addition to the relatively high Li^+ conductivity (max 1.03 mS cm^{-1}), the LIC offers structural stability and easy processability to SSBs. This study also sheds light on dry room annealed Li_3InCl_6 and provides a novel strategy to design advanced materials, using the simple and cost-effective approach with higher ionic conductivity suitable for SSBs applications. Scalable solvent-based production of LIC-based cathode coatings is possible in principle. Yet, there is room for a lot of detailed investigation and process optimization, and the solvent-free coating should be considered in future investigations due to lower costs and less environmental impact.

Data availability

Data will be made available on request.

Declaration of Competing Interest

The authors declare that they have no known competing financial interests or personal relationships that could have appeared to influence the work reported in this paper.

Acknowledgements

This work was supported and funded by EU/EURF (PASS, A76178) and EU/Interreg Nord (SolBat, grant no. 20202885) projects. The research work was also supported by the German Federal Ministry of Education and Research (BMBF) within the project FestBatt under grant number 03XP0177C and the project EProFest under grant number 03XP0346C. Sarah Mailhiot gratefully acknowledges Academy of Finland (321701) and Marie Skłodowska-Curie Actions (896824). Ville-Veikko Telkki gratefully acknowledges financial support from the European Research Council (Project number 772110) and Academy of Finland (grant no. 340099). The authors acknowledge the support of the Kvantum Institute and Center for Material Analysis at the University of Oulu.

Appendix A. Supplementary material

Supplementary data to this article can be found online at <https://doi.org/10.1016/j.matdes.2023.111690>.

References

- [1] Z. Navas-Anguita, D. García-Gusano, D. Iribarren, A review of techno-economic data for road transportation fuels, *Renew. Sustain. Energy Rev.* 112 (2019) 11–26, <https://doi.org/10.1016/j.rser.2019.05.041>.
- [2] J. Wu, L. Shen, Z. Zhang, G. Liu, Z. Wang, D. Zhou, H. Wan, X. Xu, X. Yao, All-solid-state lithium batteries with sulfide electrolytes and oxide cathodes, *Electrochem. Energy Rev.* 4 (2021) 101–135, <https://doi.org/10.1007/s41918-020-00081-4>.
- [3] H. Cavers, P. Molaiyan, M. Abdollahifar, U. Lassi, A. Kwade, Perspectives on improving the safety and sustainability of high voltage lithium-ion batteries through the electrolyte and separator region, *Adv. Energy Mater.* 12 (2022) 2200147, <https://doi.org/10.1002/aenm.202200147>.
- [4] S. Chen, D. Xie, G. Liu, J.P. Mwizerwa, Q. Zhang, Y. Zhao, X. Xu, X. Yao, Sulfide solid electrolytes for all-solid-state lithium batteries: structure, conductivity, stability and application, *Energy Storage Mater.* 14 (2018) 58–74, <https://doi.org/10.1016/j.ensm.2018.02.020>.
- [5] J. Wu, S. Liu, F. Han, X. Yao, C. Wang, Lithium/sulfide all-solid-state batteries using sulfide electrolytes, *Adv. Mater.* 33 (2021) 2000751, <https://doi.org/10.1002/adma.202000751>.
- [6] R. Sliz, P. Molaiyan, T. Fabritius, U. Lassi, Printed electronics to accelerate solid-state battery development, *Nano Express.* 3 (2022), <https://doi.org/10.1088/2632-959X/ac5d8e> 021002.
- [7] A. Manthiram, X. Yu, S. Wang, Lithium battery chemistries enabled by solid-state electrolytes, *Nat. Rev. Mater.* 2 (2017), <https://doi.org/10.1038/natrevmats.2016.103>.
- [8] G. Yang, Y. Song, Q. Wang, L. Zhang, L. Deng, Review of ionic liquids containing polymer/inorganic hybrid electrolytes for lithium metal batteries, *Mater. Des.* 190 (2020), <https://doi.org/10.1016/j.matdes.2020.108563> 108563.
- [9] P. Zhao, G. Cao, Z. Jin, H. Ming, Y. Wen, Y. Xu, X. Zhu, Y. Xiang, S. Zhang, Self-consolidation mechanism and its application in the preparation of Al-doped cubic $\text{Li}_7\text{La}_3\text{Zr}_2\text{O}_{12}$, *Mater. Des.* 139 (2018) 65–71, <https://doi.org/10.1016/j.matdes.2017.10.067>.
- [10] B. Cong, Y. Song, N. Ren, G. Xie, C. Tao, Y. Huang, G. Xu, J. Bao, Polyethylene glycol-based waterborne polyurethane as solid polymer electrolyte for all-solid-state lithium ion batteries, *Mater. Des.* 142 (2018) 221–228, <https://doi.org/10.1016/j.matdes.2018.01.039>.
- [11] N. Kamaya, K. Homma, Y. Yamakawa, M. Hirayama, R. Kanno, M. Yonemura, T. Kamiyama, Y. Kato, S. Hama, K. Kawamoto, A. Mitsui, A lithium superionic conductor, *Nat. Mater.* 10 (2011) 682–686, <https://doi.org/10.1038/nmat3066>.
- [12] Y. Kato, S. Hori, T. Saito, K. Suzuki, M. Hirayama, A. Mitsui, M. Yonemura, H. Iba, R. Kanno, High-power all-solid-state batteries using sulfide superionic conductors, *Nat. Energy.* 1 (2016) 16030, <https://doi.org/10.1038/nenergy.2016.30>.
- [13] P. Zhu, P.R. Slater, E. Kendrick, Insights into architecture, design and manufacture of electrodes for lithium-ion batteries, *Mater. Des.* 223 (2022), <https://doi.org/10.1016/j.matdes.2022.111208> 111208.
- [14] T. Asano, A. Sakai, S. Ouchi, M. Sakaida, A. Miyazaki, S. Hasegawa, Solid halide electrolytes with high lithium-ion conductivity for application in 4 V class bulk-type all-solid-state batteries, *Adv. Mater.* 30 (2018) 1803075, <https://doi.org/10.1002/adma.201803075>.
- [15] S.K. Jung, H. Gwon, G. Yoon, L.J. Miara, V. Lacivita, J.S. Kim, Pliable lithium superionic conductor for all-solid-state batteries, *ACS Energy Lett.* 6 (2021) 2006–2015, <https://doi.org/10.1021/acsenergylett.1c00545>.
- [16] X. Li, J. Liang, J. Luo, M. Norouzi Banis, C. Wang, W. Li, S. Deng, C. Yu, F. Zhao, Y. Hu, T.K. Sham, L. Zhang, S. Zhao, S. Lu, H. Huang, R. Li, K.R. Adair, X. Sun, Air-stable Li_3InCl_6 electrolyte with high voltage compatibility for all-solid-state batteries, *Energy Environ. Sci.* 12 (2019) 2665–2671, <https://doi.org/10.1039/c9ee02311a>.
- [17] C. Wang, J. Liang, M. Jiang, X. Li, S. Mukherjee, K. Adair, M. Zheng, Y. Zhao, F. Zhao, S. Zhang, R. Li, H. Huang, S. Zhao, L. Zhang, S. Lu, C.V. Singh, X. Sun, Interface-assisted in-situ growth of halide electrolytes eliminating interfacial challenges of all-inorganic solid-state batteries, *Nano Energy* 76 (2020), <https://doi.org/10.1016/j.nanoen.2020.105015>.
- [18] D. Park, H. Park, Y. Lee, S.O. Kim, H.G. Jung, K.Y. Chung, J.H. Shim, S. Yu, Theoretical design of lithium chloride superionic conductors for all-solid-state high-voltage lithium-ion batteries, *ACS Appl. Mater. Interfaces* 12 (2020) 34806–34814, <https://doi.org/10.1021/acsaami.0c07003>.
- [19] L. Zhou, C.Y. Kwok, A. Shyamsunder, Q. Zhang, X. Wu, L.F. Nazar, A new halospinel superionic conductor for high-voltage all solid state lithium batteries, *Energy Environ. Sci.* 13 (2020) 2056–2063, <https://doi.org/10.1039/d0ee01017k>.
- [20] J. Liang, X. Li, S. Wang, K.R. Adair, W. Li, Y. Zhao, C. Wang, Y. Hu, L. Zhang, S. Zhao, S. Lu, H. Huang, R. Li, Y. Mo, X. Sun, Site-occupation-tuned superionic $\text{Li}_x\text{ScCl}_{3-x}$ halide solid electrolytes for all-solid-state batteries, *J. Am. Chem. Soc.* 142 (2020) 7012–7022, <https://doi.org/10.1021/jacs.0c00134>.
- [21] H. Kwak, D. Han, J. Lyoo, J. Park, S.H. Jung, Y. Han, G. Kwon, H. Kim, S.T. Hong, K. W. Nam, Y.S. Jung, New cost-effective halide solid electrolytes for all-solid-state batteries: mechanochemically prepared Fe^{3+} -substituted Li_2ZrCl_6 , *Adv. Energy Mater.* 11 (2021) 2003190, <https://doi.org/10.1002/aenm.202003190>.
- [22] S. Zhang, F. Zhao, S. Wang, J. Liang, J. Wang, C. Wang, H. Zhang, K. Adair, W. Li, M. Li, H. Duan, Y. Zhao, R. Yu, R. Li, H. Huang, L. Zhang, S. Zhao, S. Lu, T.K. Sham, Y. Mo, X. Sun, Advanced high-voltage all-solid-state li-ion batteries enabled by a dual-halogen solid electrolyte, *Adv. Energy Mater.* 11 (2021) 2100836, <https://doi.org/10.1002/aenm.202100836>.
- [23] R.L. Sacci, T.H. Bennett, A.R. Drews, V. Anandan, M.J. Kirkham, L.L. Daemen, J. Nanda, Phase evolution during lithium-indium halide superionic conductor dehydration, *J. Mater. Chem. A* 9 (2021) 990–996, <https://doi.org/10.1039/d0ta10012a>.
- [24] S.Y. Kim, K. Kaup, K.H. Park, A. Assoud, L. Zhou, J. Liu, X. Wu, L.F. Nazar, Lithium ytterbium-based halide solid electrolytes for high voltage all-solid-state batteries, *ACS Mater. Lett.* 3 (2021) 930–938, <https://doi.org/10.1021/acsmaterialslett.1c00142>.
- [25] K. Wang, Q. Ren, Z. Gu, C. Duan, J. Wang, F. Zhu, Y. Fu, J. Hao, J. Zhu, L. He, C.W. Wang, Y. Lu, J. Ma, C. Ma, A cost-effective and humidity-tolerant chloride solid

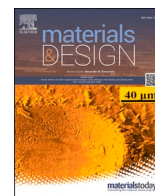
- electrolyte for lithium batteries, *Nat. Commun.* 12 (2021), <https://doi.org/10.1038/s41467-021-24697-2>.
- [26] X. Li, J. Liang, N. Chen, J. Luo, K.R. Adair, C. Wang, M.N. Banis, T. Sham, L. Zhang, S. Zhao, S. Lu, H. Huang, R. Li, X. Sun, Water-mediated synthesis of a superionic halide solid electrolyte, *Angew. Chemie.* 131 (2019) 16579–16584, <https://doi.org/10.1002/ange.201909805>.
- [27] S. Wang, X. Xu, C. Cui, C. Zeng, J. Liang, J. Fu, R. Zhang, T. Zhai, H. Li, Air sensitivity and degradation evolution of halide solid state electrolytes upon exposure, *Adv. Funct. Mater.* 32 (2022) 2108805, <https://doi.org/10.1002/adfm.202108805>.
- [28] E.O. Stejskal, J.E. Tanner, Spin diffusion measurements: spin echoes in the presence of a time-dependent field gradient, *J. Chem. Phys.* 42 (1965) 288–292, <https://doi.org/10.1063/1.1695690>.
- [29] S. Meiboom, D. Gill, Modified spin-echo method for measuring nuclear relaxation times, *Rev. Sci. Instrum.* 29 (1958) 688–691, <https://doi.org/10.1063/1.1716296>.
- [30] P. Galvosas, Y. Qiao, M. Schönhoff, P.T. Callaghan, On the use of 2D correlation and exchange NMR spectroscopy in organic porous materials, *Magn. Reson. Imaging* 25 (2007) 497–500, <https://doi.org/10.1016/j.mri.2006.11.009>.
- [31] L. Venkataramanan, Y.Q. Song, M.D. Hürlimann, Solving Fredholm integrals of the first kind with tensor product structure in 2 and 2.5 dimensions, *IEEE Trans. Signal Process.* 50 (2002) 1017–1026, <https://doi.org/10.1109/78.995059>.
- [32] K.E. Washburn, P.T. Callaghan, Tracking pore to pore exchange using relaxation exchange spectroscopy, *Phys. Rev. Lett.* 97 (2006), <https://doi.org/10.1103/PhysRevLett.97.175502> 175502.
- [33] M. Batzer, K. Voges, W. Wang, P. Michalowski, A. Kwade, Systematic evaluation of materials and recipe for scalable processing of sulfide-based solid-state batteries, *Mater. Today Commun.* 30 (2022), <https://doi.org/10.1016/j.mtcomm.2022.103189> 103189.
- [34] P.R. Rayavarapu, N. Sharma, V.K. Peterson, S. Adams, Variation in structure and Li⁺-ion migration in argyrodite-type Li₆PS₅X (X = Cl, Br, I) solid electrolytes, *J. Solid State Electrochem.* 16 (2012) 1807–1813, <https://doi.org/10.1007/s10008-011-1572-8>.
- [35] C. Fritsch, T. Zinkevich, S. Indris, M. Etter, V. Baran, T. Bergfeldt, M. Knapp, H. Ehrenberg, A.L. Hansen, Garnet to hydrogarnet: effect of post synthesis treatment on cation substituted LLZO solid electrolyte and its effect on Li ion conductivity, *RSC Adv.* 11 (2021) 30283–30294, <https://doi.org/10.1039/d1ra05961k>.
- [36] K. Hayamizu, Y. Terada, K. Kataoka, J. Akimoto, T. Haishi, Relationship between Li⁺ diffusion and ion conduction for single-crystal and powder garnet-type electrolytes studied by ⁷Li PGSE NMR spectroscopy, *Phys. Chem. Chem. Phys.* 21 (2019) 23589–23597, <https://doi.org/10.1039/c9cp04714j>.
- [37] Q. Zhao, S. Stalin, C.Z. Zhao, L.A. Archer, Designing solid-state electrolytes for safe, energy-dense batteries, *Nat. Rev. Mater.* 5 (2020) 229–252, <https://doi.org/10.1038/s41578-019-0165-5>.
- [38] R. Böhmer, K.R. Jeffrey, M. Vogel, Solid-state Li NMR with applications to the translational dynamics in ion conductors, *Prog. Nucl. Magn. Reson. Spectrosc.* 50 (2007) 87–174, <https://doi.org/10.1016/j.pnmrs.2006.12.001>.
- [39] H. Eckert, Short and medium range order in ion-conducting glasses studied by modern solid state NMR techniques, *Zeitschrift Fur Phys.Chemie* 224 (2010) 1591–1653, <https://doi.org/10.1524/zpch.2010.0030>.
- [40] C. Vinod Chandran, P. Heitjans, Solid-State NMR Studies of Lithium Ion Dynamics Across Materials Classes, in: G.A.B.T.-A.R. on N.M.R.S. Webb (Ed.), *Annu. Reports NMR Spectrosc.*, Academic Press, 2016, pp. 1–102. 10.1016/bs.arnmr.2016.03.001.
- [41] B. Stanje, D. Rettenwander, S. Breuer, M. Uitz, S. Berendts, M. Lerch, R. Uecker, G. Redhammer, I. Hanzu, M. Wilkening, Solid electrolytes: extremely fast charge carriers in garnet-type Li₆La₃ZrTaO₁₂ single crystals, *Ann. Phys.* 529 (2017) 1700140, <https://doi.org/10.1002/andp.201700140>.
- [42] K. Hayamizu, S. Seki, T. Haishi, Lithium ion micrometer diffusion in a garnet-type cubic Li₇La₃Zr₂O₁₂ (LLZO) studied using ⁷Li NMR spectroscopy, *J. Chem. Phys.* 146 (2017) 24701, <https://doi.org/10.1063/1.4973827>.
- [43] Y. Qiao, P. Galvosas, P.T. Callaghan, Diffusion correlation NMR spectroscopic study of anisotropic diffusion of water in plant tissues, *Biophys. J.* 89 (2005) 2899–2905, <https://doi.org/10.1529/biophysj.105.064709>.
- [44] R. Garcia-Mendez, J.G. Smith, J.C. Neuefeind, D.J. Siegel, J. Sakamoto, Correlating macro and atomic structure with elastic properties and ionic transport of glassy Li₂S-P₂S₅ (LPS) solid electrolyte for solid-state Li metal batteries, *Adv. Energy Mater.* 10 (2020) 2000335, <https://doi.org/10.1002/aenm.202000335>.
- [45] C.D. Reynolds, P.R. Slater, S.D. Hare, M.J.H. Simmons, E. Kendrick, A review of metrology in lithium-ion electrode coating processes, *Mater. Des.* 209 (2021), <https://doi.org/10.1016/j.matdes.2021.109971> 109971.
- [46] K. Wang, Q. Ye, J. Zhang, H. Huang, Y. Gan, X. He, W. Zhang, Halide electrolyte Li₃InCl₆-based all-solid-state lithium batteries with slurry-coated LiNi_{0.8}Co_{0.1}Mn_{0.1}O₂ composite cathode: effect of binders, *Front. Mater.* 8 (2021), <https://doi.org/10.3389/fmats.2021.727617>.

Update

Materials & Design

Volume 237, Issue , January 2024, Page

DOI: <https://doi.org/10.1016/j.matdes.2023.112435>



Corrigendum

Corrigendum to “Investigation of the structure and ionic conductivity of a Li_3InCl_6 modified by dry room annealing for solid-state Li-ion battery applications” [Mater. Design 227 (2023) 111690]

Palanivel Molaiyan^{a,*}, Sarah E. Mailhiet^{b,1}, Kevin Voges^{c,d,1}, Anu M. Kantola^b, Tao Hu^a, Peter Michalowski^{c,d}, Arno Kwade^{c,d}, Ville-Veikko Telkki^b, Ulla Lassi^{a,*}

^a Research Unit of Sustainable Chemistry, University of Oulu, 90570 Oulu, Finland

^b NMR Research Unit, University of Oulu, 90570 Oulu, Finland

^c Institute for Particle Technology, Technische Universität Braunschweig, Volkmaroder Str. 5, 38104 Braunschweig, Germany

^d Battery LabFactory Braunschweig (BLB), Technische Universität Braunschweig, Langer Kamp 19, 38106 Braunschweig, Germany

The authors regrets that, in the sub-section 3.3 Pulsed field gradient NMR (PFG-NMR), one paragraph was dropped out in the manuscript production. Here is the complete version of the subsection.

3.3. Pulsed field gradient NMR (PFG NMR)

To understand Li-ion diffusion, the LIC samples were studied by PFG-NMR. In SEs, the ion conduction pathways are composed of tortuous, nano-scale Li^+ channels through which Li^+ diffuses. PFG NMR is a non-invasive, multi-scale method for quantifying the apparent self-diffusion coefficient D , and in SEs ^7Li D studies can be used to understand ion conduction mechanisms [34].

SEs [35]. D decreases with increasing Δ for both samples due to the restricted diffusion [36]. The diffusion length z of Li scales with the measured D , such that $\langle z^2 \rangle = 2D\Delta$ (Fig. 2b). At 355 K, in the short diffusion time limit, the displacements in both samples are on the same order of magnitude, about 400 nm. This suggests that there is a relatively fast diffusion process that occurs in small domains in both LIC samples. At longer diffusion times, the diffusion process is restricted, indicated by the decreased dependence of z on Δ . Since the mean grain size is on the order of micrometers, the mean squared displacement at the longest Δ reflects the grain size. Here, the annealed LIC shows

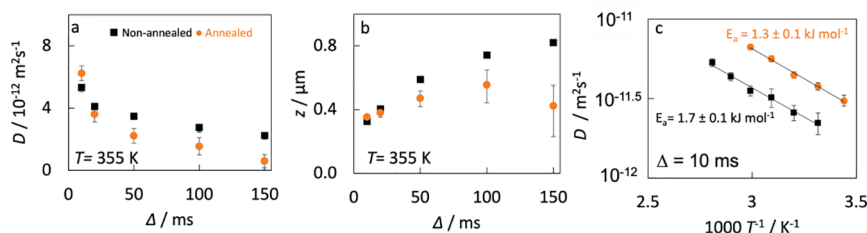


Fig. 2. (a) Diffusion coefficient of lithium ions in the LIC samples as a function of diffusion time Δ measured by ^7Li PFG NMR at 355 K and (b) the corresponding root-mean-square-displacements of the ions. (c) Diffusion coefficients as a function of temperature using a constant diffusion time of $\Delta = 10 \text{ ms}$. Data of the non-annealed and annealed LIC samples are shown by black and orange, respectively. Solid lines in (c) represent Arrhenius fits.

At the shortest diffusion time ($\Delta = 10 \text{ ms}$) and highest temperature ($T = 355 \text{ K}$), the diffusion coefficient of Li in the annealed sample is slightly higher ($6.2 \cdot 10^{-12} \text{ m}^2 \text{ s}^{-1}$) than in the non-annealed sample ($5.2 \cdot 10^{-12} \text{ m}^2 \text{ s}^{-1}$), indicating improved Li ion mobility due to annealing (Fig. 2a). The D values are slightly higher than those observed in LLZO

smaller displacement and consequently smaller grain size than the ball milled LIC.

Another measure for how Li moves across the structure is temperature-dependent D at the shortest diffusion time ($\Delta = 10 \text{ ms}$). At all temperatures, Li diffuses more quickly in the annealed LIC than in the

DOI of original article: <https://doi.org/10.1016/j.matdes.2023.111690>.

* Corresponding authors.

E-mail addresses: palaniiphys87@gmail.com (P. Molaiyan), ulla.lassi@oulu.fi (U. Lassi).

¹ These authors have the same contribution to this paper.

<https://doi.org/10.1016/j.matdes.2023.112435>

Available online 3 November 2023

0264-1275/© 2023 The Author(s). Published by Elsevier Ltd. All rights reserved.

non-annealed LIC (Fig. 2c), and the diffusion activation energy is smaller in the annealed LIC ($E_a = 1.3 \pm 0.1 \text{ kJ mol}^{-1}$) than in the non-annealed LIC ($E_a = 1.7 \pm 0.1 \text{ kJ mol}^{-1}$). Since Li-ion transport is facilitated by

impurities [37], which were observed in XRD data (Fig. 1b), it can be concluded that micrometer Li ion transport is more efficient in the annealed sample due to the increase in impurities.